

Uncertainty Propagation for Echocardiography Clinical Metric Estimation via Contour Sampling

Thierry Judge, Olivier Bernard, Woo-Jin Cho Kim, Alberto Gomez, Arian Beqiri, Agisilaos Chartsias, and Pierre-Marc Jodoin

Abstract—Echocardiography plays a fundamental role in the extraction of important clinical parameters (e.g. left ventricular volume and ejection fraction) required to determine the presence and severity of heart-related conditions. When deploying automated techniques for computing these parameters, uncertainty estimation is crucial for assessing their utility. Since clinical parameters are usually derived from segmentation maps, there is no clear path for converting pixel-wise uncertainty values into uncertainty estimates in the downstream clinical metric calculation. In this work, we propose a novel uncertainty estimation method based on contouring rather than segmentation. Our method explicitly predicts contour location uncertainty from which contour samples can be drawn. Finally, the sampled contours can be used to propagate uncertainty to clinical metrics. Our proposed method not only provides accurate uncertainty estimations for the task of contouring but also for the downstream clinical metrics on two cardiac ultrasound datasets. Code is available at: <https://github.com/ThierryJudge/contouring-uncertainty>.

Index Terms—Deep learning, Echocardiography, Segmentation, Uncertainty estimation

I. INTRODUCTION

Ultrasound imaging is the predominant modality for the assessment of cardiac function. One of the primary uses of echocardiography is the extraction of clinical metrics. For example, metrics such as left-ventricular volume and ejection fraction are widely used to diagnose heart disease. These metrics are measured by delineating the endocardial contours of the left ventricle at end-systole and end-diastole. The time-consuming nature of this task has stimulated interest in automatic methods.

Deep learning methods have proved excellent at automating the extraction of clinical metrics from echocardiographic images. Such methods can be categorized in two classes: those where the metric values are regressed directly from the input image; and those that first delineate the left ventricle and myocardium, either with a segmentation map or by contouring the endo- and epi-cardium, before computing the clinical

metrics using these segmentations. In both cases, uncertainty estimation is of great importance in clinical practice. However, both approaches have respective shortcomings.

On the one hand, uncertainty estimation of clinical metrics using regression models has been explored in [1]–[3]. However, clinicians are reluctant to use non-intelligible black-box models, hindering their adoption in practice. Moreover, these models can only estimate metrics they were explicitly trained to predict. On the other hand, many works have addressed uncertainty estimation of cardiac segmentation [4]–[6]. However, to our knowledge, no work has investigated the influence of this uncertainty on the derived clinical metrics.

The main contribution of this paper is a generalized framework to propagate uncertainty from input images to segmentation and, subsequently, to the derived clinical metrics. Unlike conventional methods yielding pixel-wise segmentation and uncertainty maps, our approach predicts aleatoric uncertainty directly for contour points. This method, combined with shape uncertainty estimates, enables sampling plausible and temporally consistent contours, and gives rise to a robust end-to-end pipeline for automatic clinical metric estimation with intelligible uncertainty.

II. RELATED WORK

A. Echocardiographic Segmentation

Recently, deep neural networks trained on publicly available datasets such as CAMUS [7] and EchoNet-Dynamic [8] have reached a performance within inter-user variability, typically using architectures based on U-Net [9]. Since, many different strategies such as echocardiography-specific data augmentation [10] and pyramid attention networks [11] have improved U-Net results. The recent publication of nnU-Net has significantly enhanced segmentation outcomes across various tasks [12] and, when applied to the CAMUS dataset, outperformed all prior methods [13].

Recent works on cardiac and lung segmentation use point-based approaches [14], [15]. This approach is viable for these organs because of their regular shape. This formulation reduces anatomical implausibilities and increases interpretability due to its similarity to human labeling. Similar work on key-point localization has also been proposed in [16], [17].

Regardless of the segmentation technique, a key objective following segmentation is the derivation of clinical metrics. A standard metric in echocardiography is the left ventricular

T. Judge and P.-M. Jodoin are with the Department of Computer Science, University of Sherbrooke, Sherbrooke, QC, Canada (e-mail: thierry.judge@usherbrooke.ca).

T. Judge and O. Bernard are with INSA, Universite Claude Bernard Lyon 1, CNRS UMR 5220, Inserm U1206, CREATIS, Villeurbanne, France.

W.-J. Cho Kim, A. Gomez, A. Beqiri and A. Chartsias are with Ultrasonics Ltd., Oxford, OX4 2SU, UK

A. Gomez is with King's College London, London, WC2R 2LS, UK

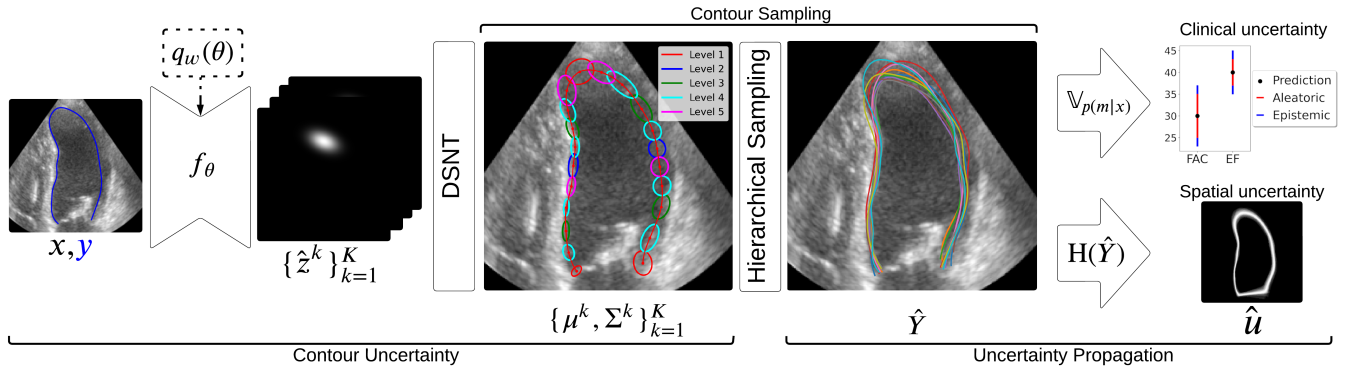


Fig. 1: Schematic of the CASUS framework illustrating the three core components: (1) prediction of contour point uncertainty, (2) a contour sampling mechanism, and (3) propagation of sampled contour uncertainties to compute clinical metrics.

area. A more accurate evaluation of the ventricular cavity size involves determining the ventricular volume using Simpson’s biplane method [18], utilizing the segmentation obtained from the apical 4-chamber (A4C) and apical 2-chamber (A2C) views. Additionally, temporal metrics are of significant interest. Examining the ratio of heart size between end-systole (ES) and end-diastole (ED) can provide indications of certain cardiac pathologies. The fractional area change (FAC) is defined as the difference between the end-diastolic area and the end-systolic area, divided by the end-diastolic area. Ejection fraction (EF) is calculated similarly, albeit with volume measurements.

B. Uncertainty Estimation

Although numerous studies have proposed new models to enhance the segmentation accuracy, relatively few have addressed the predictive uncertainty of these models. Accounting for uncertainty is crucial, as although neural networks can achieve human-level performance, they can also make occasional critical errors.

Uncertainty is usually classified into two categories: *aleatoric* and *epistemic* [19]. Aleatoric uncertainty is the uncertainty present within the data itself. In medical imaging, aleatoric uncertainty is caused by the inherent ambiguity of images, which for instance can occur due to noisy images or labels. Epistemic uncertainty is the uncertainty associated with the model and is caused by the limited size of the training dataset. While epistemic uncertainty can be reduced by acquiring more data, aleatoric uncertainty is irreducible.

One prominent approach for modeling epistemic uncertainty involves characterizing the distribution of model weights, θ , conditioned on the data \mathcal{D} . This posterior distribution over weights, $p(\theta|\mathcal{D})$, is generally intractable to compute analytically for neural networks. Variational inference offers a method to approximate the true posterior using a variational distribution, $q_w(\theta)$, in Bayesian neural networks [20]. However, this approach necessitates significant modifications to standard training procedures. Alternative methods, such as Monte-Carlo (MC) dropout, have demonstrated effectiveness as a practical approximation for Bayesian neural networks,

allowing for uncertainty estimation without altering the training pipeline, and have achieved reliable results [21], [22]. On the other hand, a frequentist approach with ensemble methods leverages the variability of independently trained networks—each trained on different data subsets or with distinct hyperparameters—to capture uncertainty [23].

While epistemic uncertainty methods usually do not require any data assumptions, this is not the case for aleatoric uncertainty methods. Most commonly, probabilistic approaches that model a distribution are used in aleatoric uncertainty methods. Most commonly, probabilistic approaches that model a parameterized distribution $p_\theta(y|x)$ over the output y given the input x are employed in aleatoric uncertainty methods. For instance, in the case of univariate regression, the mean and variance of a Gaussian distribution are learned by maximizing the negative log-likelihood with respect to both parameters. This can be extended to the multivariate normal [24] or with different distributions such as the skew-normal distribution [25]. In the case of classification, uncertainty is approximated by modeling a Gaussian distribution across every output logit [19].

Aleatoric uncertainty can also be predicted with non-probabilistic methods. Methods that use test-time augmentation apply random data transformations, perform inference and aggregate the outputs to model uncertainty [26].

While modeling both aleatoric and epistemic uncertainty is relevant to understanding the origin of the prediction ambiguity, it is also important to model the full predictive uncertainty. If the aleatoric uncertainty is captured by a model $p_\theta(y|x)$ and the epistemic uncertainty is modeled by $q_w(\theta)$, the predictive uncertainty is given by the law of total variance [19]

$$\mathbb{V}_{p(y|x)} = \mathbb{E}_{q_w(\theta)} \left[\mathbb{V}_{p_\theta(y|x)}[y] \right] + \mathbb{V}_{q_w(\theta)} \left[\mathbb{E}_{p_\theta(y|x)}[y] \right]. \quad (1)$$

1) *Segmentation uncertainty*: In many cases, segmentation uncertainty is tackled similarly to classification. Epistemic uncertainty methods, such as MC dropout and ensembles, do not require any changes as multiple forward passes generate varying segmentation maps. In the case of aleatoric uncertainty, a simple way is to consider the prediction for each pixel as an independent classifier and estimate aleatoric uncertainty by modeling the logits of each pixel with a Gaussian [19].

Pixel-wise aleatoric uncertainty often performs poorly since independent pixel distributions make plausible segmentation samples unlikely. For this reason, methods such as Probabilistic U-Net [27] and Phi-Seg [28] use a variational autoencoder coupled with a segmentation network to learn a distribution of shapes in the latent space from which plausible samples can be drawn. Similarly, stochastic segmentation networks learn a low-rank multivariate Gaussian representation of pixel distributions, enabling efficient training despite the large covariance matrix, and outperform previous methods [29].

Finally, test-time augmentation can be extended to segmentation by applying transforms to the input image and applying the inverse transform on the output segmentation [30].

2) *Uncertainty in echocardiographic image analysis*: Numerous approaches have been developed to estimate uncertainty in echocardiography, usually focusing on segmentation or clinical metric prediction. For the former task, techniques like ensembles and test-time augmentation have been shown to improve left-ventricle segmentation performance (as measured by Dice scores) by excluding the most uncertain samples [6]. Judge *et al.* took a post-hoc approach, predicting segmentation uncertainty by encoding prior information in a shared latent space [5]. For the latter task, Behnami *et al.* [3] proposed a multitask learning approach to estimate EF alongside its uncertainty for both the A2C and A4C views, using Gaussian modeling. Their work also included a classification-based prediction of EF, categorizing cardiac function into four classes from normal to severe dysfunction. In a similar vein, Kazemi Esfeh *et al.* introduced a sampling-free ensemble method to estimate epistemic uncertainty, specifically targeting EF regression with a delta ensemble approach [2].

Although these methods may propose robust prediction and uncertainty measures, they lack intelligibility of clinical metric prediction extracted from segmentation maps. Jafari *et al.* [31] proposed a method to estimate segmentation uncertainty using MC dropout. They then define an uncertainty measure based on this uncertainty map and use it to filter samples showing an increased correlation between predicted ejection fraction values and ground truth values. While this is similar to our work, there is no explicit uncertainty estimation for the ejection fraction as their method only filters out samples with uncertainty above a certain threshold.

In summary, existing methods have failed to connect uncertainty for segmentation and the resulting clinical metrics. This paper addresses this limitation by providing a method to quantify and propagate uncertainty from the predicted shape to the derived metrics in an interpretable way.

III. METHOD

A standard segmentation pipeline for estimating clinical metrics in echocardiographic images requires a dataset consisting of N pairs $\{x_n, y_n\}_{n=1}^N$, where each pair is an image $x_n \in \mathbb{R}^{H \times W}$ of height H and width W , and corresponding ground truth segmentation map of C classes $y_n \in \{0, 1\}^{C \times H \times W}$. This dataset is used to train a segmentation network f_θ^{seg} . For a given input image, x_n , the segmentation network outputs a segmentation map $\hat{y}_n = f_\theta^{seg}(x_n)$. Given one (or many)

segmentation maps $\hat{y}_n \in \{0, 1\}^{C \times H \times W}$, a clinical metric $F(\cdot)$ is computed, e.g the area of a segmentation map or the left ventricle ejection fraction given the 2CH and 4CH view segmentation for the ES and ED frames.

We aim to estimate the uncertainty of clinical metrics by propagating the uncertainty from segmentation maps or contours, the latter of which is the focus of this paper. Our method, Contour Aleatoric Shape Uncertainty Sampling (CASUS), is illustrated in Figure 1 and contains three main components. The first is the contour uncertainty prediction, where a neural network is trained to predict points defining the contour of the left-ventricle and their uncertainty. The second component is a hierarchical contour sampling algorithm that allows for the sampling of plausible contours from independent point predictions. This sampling process relies on a conditional shape model that allows the modeling of shape uncertainty. Finally, the third step propagates the uncertainty from the contour uncertainty prediction to the clinical metrics.

A. Contour-based Aleatoric Uncertainty Modeling

Contrary to most previous work in uncertainty estimation for segmentation, we model the uncertainty of contour points rather than the pixel-wise uncertainty. We advocate that this is more appropriate for left-ventricle segmentation as there is no uncertainty around the presence of the left-ventricle in the image, but rather uncertainty regarding its position. This aspect of our work focuses on estimating aleatoric uncertainty, as epistemic uncertainty methods are well-established and usually task-agnostic. Our method can be combined with epistemic uncertainty methods, as shown in Section III-D.

The prediction of a contour and its associated uncertainty begins with a training dataset made of $\mathcal{D} = \{x_n, s_n\}_{n=1}^N$, where s_n is a series of K ordered points s_n^k drawn by an expert or extracted from a segmentation maps. With \mathcal{D} , a contouring neural network $f_\theta^c(\cdot)$ is trained to predict K heatmaps $Z^k \in \mathbb{R}^{H \times W}$, each associated to a control point, as illustrated on the left of Figure 1. Each heatmap contains a blurry white spot whose center corresponds to the position of a control point (variable μ) and whose halo size corresponds to the uncertainty of that point (variable Σ). The heatmaps are normalized in 2D to obtain \hat{Z}^k , such that it represents a probability density function for the coordinates c^k of a given point k in the shape.

We build upon the differentiable spatial to numerical transform (DSNT) [32] to extract the parameters of a 2D Gaussian from the heatmap. To extract the mean and variance of the heatmap for each point, two coordinate maps $\mathbf{I} \in \mathbb{R}^{H \times W}$ and $\mathbf{J} \in \mathbb{R}^{H \times W}$, where $\mathbf{I}_{i,j} = \frac{2j-(W+1)}{W}$ and $\mathbf{J}_{i,j} = \frac{2i-(H+1)}{H}$ are used. The mean and variance can be extracted as follows,

$$\hat{\mu}^k = \mathbb{E}[c^k] = \left[\langle \hat{Z}^k, \mathbf{I} \rangle_F, \langle \hat{Z}^k, \mathbf{J} \rangle_F \right] \in \mathbb{R}^2, \quad (2)$$

$$\begin{aligned} \mathbb{V}[c^{k_j}] &= E[(c^{k_j} - E[c^{k_j}])^2] \\ &= \langle \hat{Z}^k, (\mathbf{I} - \mu^{k_j}) \odot (\mathbf{I} - \mu^{k_j}) \rangle_F \in \mathbb{R}, \end{aligned} \quad (3)$$

where $\langle \cdot, \cdot \rangle_F$ is the Frobenius inner product, \odot corresponds to the Hadamard product, and $\mathbb{V}[c^{k_i}]$ is computed similarly. The

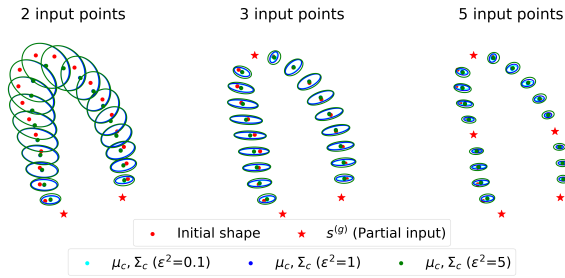


Fig. 2: Example of the posterior shape model output for various partial inputs of a given left ventricle shape for different slack parameter values (ϵ^2).

covariance can also be extracted from the heatmap,

$$\begin{aligned} \mathbb{C}[c^k] &= E[(c^{k_j} - E[c^{k_j}])(c^{k_i} - E[c^{k_i}])] \\ &= \langle \hat{Z}, (\mathbf{I} - \mu^{k_j}) \odot (\mathbf{J} - \mu^{k_i}) \rangle_F \in \mathbb{R}. \end{aligned} \quad (4)$$

By combining the computed variance and covariance values, the covariance matrix can be constructed and a 2-dimensional Gaussian distribution can be modeled.

$$\hat{\Sigma}^k = \begin{bmatrix} \mathbb{V}[c^{k_j}] & \mathbb{C}[c^{k_j}] \\ \mathbb{C}[c^{k_i}] & \mathbb{V}[c^{k_i}] \end{bmatrix} \in \mathbb{R}^{2 \times 2} \quad (5)$$

The model thus predicts a tuple $(\hat{\mu}, \hat{\Sigma})$ for each image x , with $\hat{\mu} \in \mathbb{R}^{K \times 2}$ and $\hat{\Sigma} \in \mathbb{R}^{K \times 2 \times 2}$ (c.f. Fig. 1 middle). To train the network, the negative-log likelihood of the Gaussian is used for each point,

$$\mathcal{L} = \frac{1}{NK} \sum_{n=1}^N \sum_{k=1}^K \frac{1}{2} \log |\hat{\Sigma}_n^k| + \frac{1}{2} (\hat{\mu}_n^k - s_n^k)^T (\hat{\Sigma}_n^k)^{-1} (\hat{\mu}_n^k - s_n^k)$$

B. Shape Uncertainty Modeling

While the previous formulation allows predicting one contour, the uncertainty propagation to clinical metrics requires multiple contours, which can be retrieved with stochastic sampling of $\{\hat{\mu}^k, \hat{\Sigma}^k\}_{k=1}^K$. However, sampling each individual distribution $\{\hat{\mu}^k, \hat{\Sigma}^k\}$ does not provide valid contours as the inter-point covariance is not modeled. The entire shape distribution requires predicting a $2K \times 2K$ covariance, which is numerically unstable. We thus propose using a shape model to model the shape uncertainty between points.

We do this with a statistical shape model that models the uncertainty of points given the position of other points. To define the conditional distribution we use a posterior shape model (PSM) based on principal component analysis (PCA), that predicts conditional distributions given partial data [33]. We start by introducing the PCA notation used in the PSM.

PCA: Given a set of N shapes $\mathbf{S} = \{s_1, s_2, \dots, s_N\}$, each containing K 2D points, $s_n \in \mathbb{R}^{2K}$, i.e. the training set used for contouring, the mean, $\bar{\mu} \in \mathbb{R}^{2K}$ and covariance matrix, $\bar{\Sigma} \in \mathbb{R}^{2K \times 2K}$ of these N shapes can be computed as follows,

$$\bar{\mu} = \frac{1}{N} \sum_{i=n}^N s_n, \quad \bar{\Sigma} = \frac{1}{N} \sum_{n=1}^N (s_n - \bar{\mu})(s_n - \bar{\mu})^T. \quad (6)$$

By performing the eigenvalue decomposition of the covariance matrix, $\bar{\Sigma} = U\Lambda^2U^T$, all shapes can be represented by

$$s = s(\alpha) = \bar{\mu} + U\Lambda\alpha = \bar{\mu} + Q\alpha. \quad (7)$$

If $\alpha \sim \mathcal{N}(0, I)$, the shapes $s(\alpha) = \bar{\mu} + Q\alpha$ are distributed according to $\mathcal{N}(\bar{\mu}, \bar{\Sigma})$.

PSM: The goal of the posterior shape model is to produce a conditional distribution given partial data. More formally, given partial information, i.e. a selected subset of points $s^{(g)} \in \mathbb{R}^{2q}$, where $q < K$, the goal is to estimate $p(s|s^{(g)})$. Per [33], the conditional distribution is a multivariate Gaussian,

$$p(s|s^{(g)}) = \mathcal{N}(\mu_c, \Sigma_c). \quad (8)$$

The mean and covariance matrix are given by

$$\mu_c = \bar{\mu} + Q(Q_g^T Q_g + \epsilon^2 I_{2K})^{-1} Q_g^T (s^{(g)} - \mu_g) \in \mathbb{R}^{2K}, \quad (9)$$

$$\Sigma_c = \epsilon^2 Q(Q_g^T Q_g + \epsilon^2 I_{2K})^{-1} Q_g^T \in \mathbb{R}^{2K \times 2K}, \quad (10)$$

where $\mu_g \in \mathbb{R}^{2q}$ is the sub-vector of $\bar{\mu}$ for corresponding entries of $s^{(g)}$, $Q_g \in \mathbb{R}^{2q \times 2K}$ is the sub-matrix of rows of Q for corresponding entries of $s^{(g)}$ and ϵ^2 is a slack term to account for variations in data from the original training set.

While the PSM is defined to use the mean $\bar{\mu}$ of the shape set to compute Q and in Equation (9) and Equation (10), we instead use $\hat{\mu}$ as this allows the PSM to model the possible variations in the dataset, and therefore the shape uncertainty, with respect to the predicted shape. We will refer to the matrix Q computed with respect to $\hat{\mu}$ as \hat{Q} . We will denote the operation of computing the conditional distribution given a partial input as follows,

$$\mu_c, \Sigma_c = \text{PSM}(s^{(g)}, \hat{\mu}, \hat{Q}). \quad (11)$$

An example of the PSM on the shape of the left ventricle is illustrated in Figure 2 showing that points close to the partial input have low variance. Also, as the size of the partial input increases, the uncertainty over the remaining points' positions is lower therefore restricting the possible positions.

C. Aleatoric and Shape Uncertainty Fusion

Given appropriate methods for modeling both the aleatoric contour uncertainty and the shape uncertainty, we can propose an algorithm to sample multiple contours. We do this by defining a hierarchical sampling algorithm that fuses both the contour uncertainty and shape uncertainty.

By the very nature of the data and labeling process of the left-ventricle shape, it can be assumed that only the apex and the two basal points are independent. These points are tied to well-defined anatomical landmarks: the basal points are located at the base of the mitral valve and the apex is the farthest point from these points, located at the tip of the left ventricle. The other points in the shape are present to define the contour along the endocardial border but do not have a true anatomical landmark in the image.

Our hierarchical sampling process therefore begins by sampling both basal points and apex point independently. Their position is then used to define a conditional distribution that is used to update the neural network's prediction.

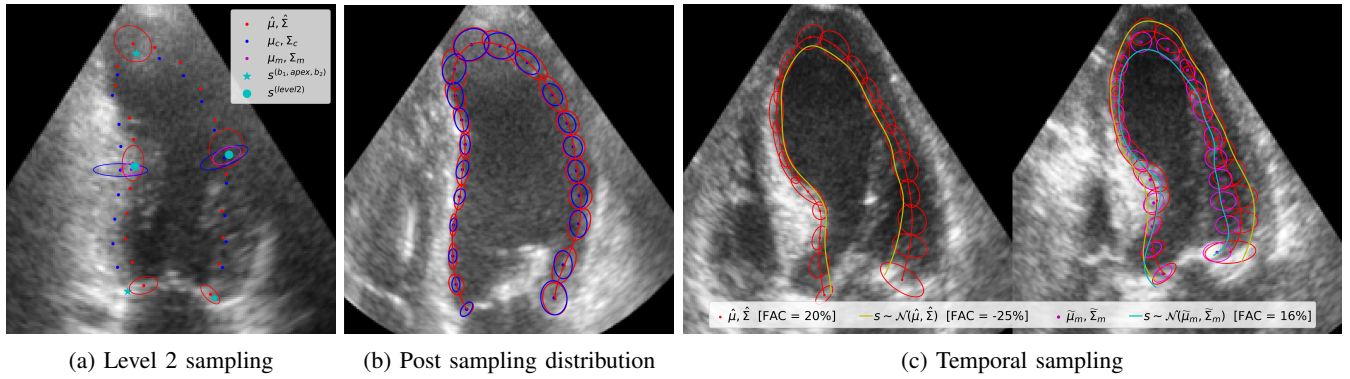


Fig. 3: (a) Example of the sampling process. Given the initial points (cyan stars), the posterior shape model output (blue) is merged with the predicted distribution (red) to obtain a distribution (magenta) from which points are sampled (cyan). (b) The predicted contour and uncertainty distributions in red and the points sampled with the PSM sampler in blue. (c) Temporal consistent sampling. The yellow curve shows an example of the failure case of independent sampling where the ED area (left) is larger than the ES area (right) resulting in a negative FAC greatly differing from the mean prediction. The time-consistent sampling produces distributions (magenta) that are consistent with the ES contour, resulting in a plausible contour for ED (cyan).

To sample a shape s given the outputs of the uncertainty contouring model, $\{\hat{\mu}^k, \hat{\Sigma}^k\}_{k=1}^K$, the apex is initially sampled,

$$s^{(\text{apex})} \sim \mathcal{N}(\hat{\mu}^{(\text{apex})}, \hat{\Sigma}^{(\text{apex})}). \quad (12)$$

The same is done for both basal points (b_1 and b_2). Given this partial input, the parameters of the posterior shape model distribution can be predicted

$$\mu_c, \Sigma_c = \text{PSM}(s^{(b_1, \text{apex}, b_2)}, \hat{\mu}, \hat{Q}). \quad (13)$$

To obtain a distribution conditioned on both the original model prediction and the sampled points we fuse the contour uncertainty distributions and the shape uncertainty given by the posterior shape model distribution. We merge both distributions by multiplying them as is done when combining a likelihood and prior term. The multiplication of the two multivariate Gaussians is defined as follows

$$\mu_m^k = \hat{\Sigma}^k (\hat{\Sigma}^k + \Sigma_c^k)^{-1} \mu_c^k + \Sigma_c^k (\hat{\Sigma}^k + \Sigma_c^k)^{-1} \hat{\mu}^k, \quad (14)$$

$$\Sigma_m^k = \hat{\Sigma}^k (\hat{\Sigma}^k + \Sigma_c^k)^{-1} \Sigma_c^k, \quad (15)$$

where Σ_c^k is 2×2 sub-matrix extracted from Σ_c along the diagonal at the indices corresponding to point k . With a new conditioned distribution for each point, we sample the midpoints between the previously sampled points and repeat the process until all points are sampled at each hierarchical level (shown in Figure 1).

The second sampling level of the hierarchical sampling process is illustrated in Figure 3a. In Figure 3b, the final point distribution is compared with the original predicted distribution showing that the PSM sampler does not alter the point distribution except for the points sampled last.

1) Temporal consistent sampling: One critical consideration in cardiac ultrasound is the temporal aspect, as many clinical parameters are derived from segmented data at distinct time points. As our contouring method makes independent predictions for the ES and ED frames, as is the case for most segmentation methods, there is a risk of obtaining sets

of contours that lack physiological plausibility. For instance, sampling a contour inside the mean contour during end-diastole (when the left ventricle is at its largest) and another contour outside the mean contour during end-systole (when the left ventricle is at its smallest) could result in a negative FAC, which contradicts physiological norms.

To reduce the occurrence of implausible samples while sampling, we use the posterior shape model to restrict the distribution of the contour sampled at the second time instant. To do so, we consider the set of shapes for ES and ED instants $\tilde{\mathbf{S}} \in \mathbb{R}^{N \times 4K}$. We compute the mean $\tilde{\mu} \in \mathbb{R}^{4K}$ and covariance matrix $\tilde{\Sigma} \in \mathbb{R}^{4K \times 4K}$ of this set, from which we can extract the PCA parameter \tilde{Q} . We then sample the first contour from the ED predictions with the hierarchical sampling process. We compute the posterior shape model parameters using, Equation (9) and Equation (10), to obtain $\tilde{\mu}_c$ and $\tilde{\Sigma}_c$. We merge the predicted distribution for the ES with the PSM output with Equation (14) and Equation (15) to obtain $\tilde{\mu}_m$ and $\tilde{\Sigma}_m$ from which a contour is derived with hierarchical sampling. In practice, the first sampled contour is randomly chosen between the ES and ED frame. An example of the sequential sampling process is shown in Figure 3c.

D. Uncertainty Propagation

In the previous two subsections, we presented a contour aleatoric uncertainty estimation method. This method allows to model the distribution of plausible samples for a given image which we denote as $p_\theta(s|x)$, where s is a left-ventricle shape and x is the input ultrasound image. To allow for this section of the paper to be compared with standard segmentation methods, we consider the segmentation map obtained by filling the inside of a contour s and denote it y . Assuming we have an approximated posterior distribution for the neural network weights, $q_w(\theta)$, we can propagate both the aleatoric and epistemic segmentation uncertainty to the clinical metrics.

If the value of a certain clinical metric F is given by $m = F(y)$ where y is a segmentation map, the predictive

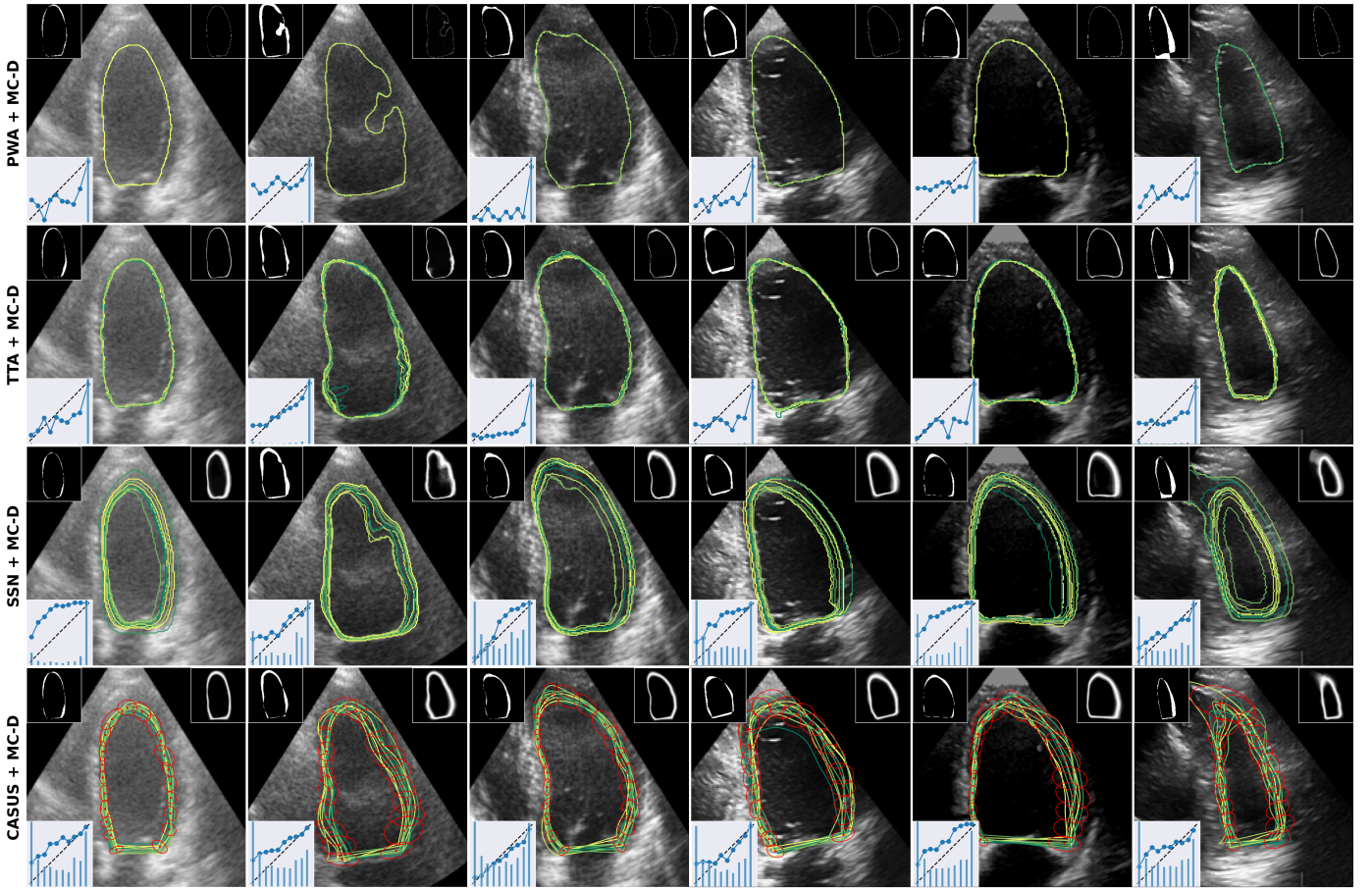


Fig. 4: Example predictions from different methods. Each row corresponds to a different method and each column a specific image. In each image, 10 samples are shown. The top left and right sub-images are the pixel-wise error and uncertainty maps, respectively. For each image, the pixel-wise calibration reliability diagram is plotted in the bottom left corner. The histogram indicates the number of samples in each bin. The last row corresponds to the CASUS method, where the red ellipses correspond to 95% confidence intervals for the location of each point.

uncertainty, i.e. the sum of the aleatoric and epistemic uncertainty, of m is given by

$$\mathbb{V}_{p(m|x)} = \mathbb{E}_{q_w(\theta)} \left[\mathbb{V}_{p_\theta(y|x)} [F(y)] \right] + \mathbb{V}_{q_w(\theta)} \left[\mathbb{E}_{p_\theta(y|x)} [F(y)] \right].$$

In the case where only epistemic uncertainty is computed (i.e. $p_\theta(y|x)$ is a point estimate), the first term will be zero. Conversely, if $q_w(\theta)$ is a point estimate, no epistemic uncertainty is estimated.

To compute this uncertainty, we use a Monte Carlo framework. We define T_a to be the number of samples to estimate the aleatoric uncertainty and T_e to be the number of epistemic samples. We compute a series of predictions

$$\hat{Y} = \{(\hat{y}_1^1, \hat{y}_2^1, \dots, \hat{y}_{T_a}^1), \dots, (\hat{y}_1^{T_e}, \hat{y}_2^{T_e}, \dots, \hat{y}_{T_a}^{T_e})\}, \quad (16)$$

where $\hat{y}_j^i \sim p_{\theta^i}(y|x)$ with $\theta^i \sim q_w(\theta)$. For each prediction in \hat{Y} , a given clinical metric F can be computed to obtain

$$M = \{(m_1^1, m_2^1, \dots, m_{T_a}^1), \dots, (m_1^{T_e}, m_2^{T_e}, \dots, m_{T_a}^{T_e})\}, \quad (17)$$

where $m_j^i = F(\hat{y}_j^i)$. The mean and variance of each subset are computed to obtain

$$M' = \{(\mu_{m^1}, \sigma_{m^1}^2), \dots, (\mu_{m^{T_e}}, \sigma_{m^{T_e}}^2)\}. \quad (18)$$

For the input image and metric, we compute the mean, μ_F , as well as the aleatoric $\sigma_{F_a}^2$ and epistemic $\sigma_{F_e}^2$ uncertainties

$$\mu_F = \mathbb{E}_i[\mu_i], \quad \sigma_{F_a}^2 = \mathbb{E}_i[\sigma_i^2], \quad \sigma_{F_e}^2 = \mathbb{V}_i[\mu_i]. \quad (19)$$

Finally, both components of the clinical metric uncertainty can be combined to obtain the predictive uncertainty.

$$\sigma_F^2 = \sigma_{F_a}^2 + \sigma_{F_e}^2. \quad (20)$$

The spatial uncertainty can be estimated per pixel by computing entropy of all samples in \hat{Y} ,

$$\hat{u} = H(\hat{Y}) = -\frac{1}{\log C} \sum_{c=1}^C \bar{y}_c \log \bar{y}_c \in [0, 1]^{H \times W} \quad (21)$$

where $\bar{y} = \frac{1}{T} \sum_{t=1}^T \hat{Y}_t \in \mathbb{R}^{C \times H \times W}$ is the mean of all samples with $T = T_a \cdot T_e$.

IV. EXPERIMENTAL SETUP

A. Data

1) **CAMUS**: The CAMUS dataset, as detailed in the work by Leclerc et al. [7], encompasses conventional clinical examinations derived from 500 patients and acquired using a

Method		CAMUS				Private Card. US			
Aleatoric	Epistemic	Dice ↑	Corr. ↑	ECE↓	MI↑	Dice↑	Corr.↑	ECE↓	MI↑
PWA	-	.932±.001	.057±.019	.045±.005	.135±.006	.876±0.004	.139±.110	.282±.009	0.127±0.005
TTA	-	.931±.002	.252±.022	.044±.003	.209±.004	.873±0.003	.421±.046	.073±.001	0.199±0.005
SSN	-	.927±.005	.172±.060	.085±.022	.188±.012	.868±0.004	.233±.055	.168±.030	0.204±0.009
CASUS	-	.934±.003	.666±.142	.083±.008	.189±.003	.875±0.005	.609±.162	.102±.007	0.211±0.005
CASUS+t	-	.934±.003	.674±.138	.080±.009	.200±.008	.875±0.005	.606±.147	.093±.007	0.222±0.005
-	MC-D.	.931±.002	.071±.051	.042±.005	.156±.017	.875±0.002	.138±.039	.076±.005	0.155±0.012
PWA	MC-D.	.933±.000	.065±.050	.044±.000	.131±.012	.880±0.003	.018±.061	.083±.006	0.126±0.014
TTA	MC-D.	.932±.002	.338±.094	.047±.003	.214±.005	.875±0.002	.472±.045	.083±.002	0.206±0.005
SSN	MC-D.	.928±.002	.181±.089	.104±.039	.173±.015	.874±0.004	.240±.094	.205±.051	0.178±0.014
CASUS	MC-D.	.934±.001	.624±.046	.090±.001	.178±.003	.879±0.001	.588±.113	.108±.006	0.198±0.004
CASUS+t	MC-D.	.934±.001	.652±.047	.086±.003	.188±.002	.879±0.001	.558±.092	.097±.006	0.209±0.004

TABLE 1: Mean and standard deviation values segmentation results (5 random seeds). Best and second best results are highlighted in red and blue respectively.

GE Vivid E95 ultrasound scanner. The imaging acquisitions were specifically tailored for the assessment of left ventricular ejection fraction. Each patient’s dataset includes 2D A4C and A4C view sequences, employing a consistent acquisition protocol and exported from the EchoPAC analysis software (GE Vingmed Ultrasound, Horten, Norway).

A senior cardiologist annotated the endocardium and epicardium borders of the left ventricle, as well as the atrium, for both ED and ES images in the dataset. The dataset is partitioned into 400 training patients, 50 validation patients, and 50 testing patients. Contour points were defined by identifying the endocardium basal points, followed by determining the apex as the farthest point along the respective edges. Each contour is composed of 21 points.

2) *Private dataset*: The dataset is derived from the EVAREST trial [34], a comprehensive multi-site, multi-vendor study conducted in the UK. A2C and A4C echocardiograms were acquired from patients at rest or under induced stress. The dataset includes healthy individuals and patients with conditions such as coronary artery disease and COVID.

The dataset is divided into a training/validation set (80/20 split) and an independent test set sourced from different sites. It consists of 994 echocardiograms from 684 patients for the training/validation set and 368 echocardiograms from 206 patients for the independent test set. Expert annotations for the endocardium contour were performed, with a minimum of 7 points labeled based on perceived anatomical landmarks. Additional points were added as needed to precisely delineate the contour, and the contours were subsequently resampled to include a total of 21 points evenly distributed along the contour.

B. Model Configuration

To evaluate both our uncertainty propagation framework and our contour sampling method, we implemented a variety of aleatoric uncertainty methods for segmentation. We compared our method to pixel-wise aleatoric uncertainty (PWA) [19], stochastic segmentation networks (SSN) [29] and test-time augmentation (TTA) [30]. We also evaluate our method

(CASUS), and our method with the temporal consideration described in Section III-C.1 (CASUS-t). We also compare with epistemic uncertainty using Monte-Carlo Dropout (MC-D). Finally, we combine both aleatoric and epistemic uncertainty for all combinations of aleatoric and epistemic methods. For all methods, we use a 2D U-Net model defined in [13] and resized images to 256x256. All methods were trained with a batch size of 32 for a maximum of 1000 epochs with early stopping after 100 epochs without validation loss improvement. The Adam optimizer [35] was used for all methods except for the stochastic segmentation network that was only trainable with RSM-prop which is in the original code provided by the authors. We trained using data augmentation, which included random rotations and translations, random brightness and contrast changes, and finally, random Gamma corrections. We used the same data augmentation for the test-time augmentations.

We generated samples with $T_a = 25$ and $T_e = 10$, except for the MC-Dropout only method where $T_e = 25$. We applied post processing to both the mean prediction and the Monte-Carlo samples for all segmentation based methods to remove holes and select only the largest predicted structure.

C. Evaluation Metrics

1) *Segmentation metrics*: For the segmentation metrics, we consider the output segmentation map, as well as the uncertainty map, predicted using Equation (21). We used the Dice coefficient to assess the segmentation quality. To assess the quality of the uncertainty map we consider the image-level uncertainty estimate by computing the mean of the uncertainty map weighted by the size of the prediction and pixel-level uncertainty where the raw pixel uncertainty values are used. The metric used to assess the image level uncertainty is the negative correlation (Corr.) between image-level uncertainty and the image Dice. To evaluate the pixel-wise calibration of the uncertainty maps the expected calibration error (ECE) is computed as follows [36]:

$$ECE = \sum_{m=1}^M \frac{|B_m|}{N_{test}} |\text{acc}(B_m) - \text{conf}(B_m)| \quad (22)$$

Method		CAMUS				Private Card. US			
Aleatoric	Epistemic	Area	FAC	Volume	EF	Area	FAC	Volume	EF
PWA	-	3114 \pm 115	45.7 \pm 1.9(0.8)	59.7 \pm 2.7	21.8 \pm 2.5(0.0)	30968 \pm 1718	366.3 \pm 12.6(3.6)	550.6 \pm 9.3	156.9 \pm 7.0(0.8)
TTA	-	2685 \pm 166	32.9 \pm 3.9(0.8)	58.4 \pm 3.7	15.9 \pm 3.2(0.0)	24565 \pm 538	281.2 \pm 12.6(3.6)	454.1 \pm 17.2	135.9 \pm 5.7(0.9)
SSN	-	1866 \pm 615	57.4 \pm 6.6(0.2)	25.7 \pm 4.0	18.9 \pm 3.5(0.0)	11528 \pm 6290	312.9 \pm 58.6(6.2)	156.7 \pm 48.6	68.7 \pm 18.5(2.5)
CASUS	-	539 \pm 194	18.4 \pm 3.9(0.6)	13.5 \pm 6.9	8.4 \pm 2.2(0.0)	10546 \pm 1179	42.0 \pm 4.1(3.6)	250.3 \pm 34.6	22.1 \pm 2.2(0.8)
CASUS+t	-	609 \pm 153	10.0 \pm 2.0(0.4)	17.3 \pm 5.2	6.0 \pm 0.5(0.0)	8680 \pm 608	49.4 \pm 8.6(2.7)	219.0 \pm 27.0	36.4 \pm 6.1(0.0)
-	MC-D	3460 \pm 169	48.6 \pm 4.4(0.8)	72.1 \pm 7.3	27.4 \pm 4.8(0.4)	30570 \pm 790	374.2 \pm 12.2(3.9)	579.8 \pm 28.9	182.6 \pm 5.1(1.2)
PWA	MC-D	3101 \pm 96	46.6 \pm 4.0(0.8)	57.9 \pm 2.8	23.1 \pm 3.6(0.0)	28914 \pm 1438	351.1 \pm 15.4(3.3)	508.3 \pm 26.9	151.2 \pm 8.1(0.5)
TTA	MC-D	2430 \pm 203	28.1 \pm 3.8(1.2)	48.1 \pm 7.8	14.2 \pm 4.0(0.4)	22757 \pm 1153	250.7 \pm 7.6(0.0)	417.7 \pm 26.3	115.0 \pm 5.1(0.0)
SSN	MC-D	3618 \pm 1241	87.3 \pm 19.1(0.8)	46.7 \pm 16.9	30.3 \pm 7.0(0.0)	25388 \pm 8890	535.6 \pm 113.1(4.3)	267.3 \pm 174.9	149.2 \pm 37.4(1.5)
CASUS	MC-D	499 \pm 145	27.6 \pm 1.6(0.8)	12.7 \pm 1.9	13.6 \pm 1.5(0.0)	5365 \pm 1177	80.8 \pm 9.7(2.9)	147.5 \pm 37.7	34.0 \pm 9.6(0.7)
CASUS+t	MC-D	420 \pm 122	15.2 \pm 2.5(0.6)	11.6 \pm 4.8	8.4 \pm 1.0(0.0)	4577 \pm 1041	31.6 \pm 7.9(2.7)	118.2 \pm 28.4	23.8 \pm 8.4(0.0)

TABLE II: Mean and standard deviation for uncertainty calibration error values (5 random seeds). Best and second best results are highlighted in red and blue respectively. The average percentage of rejected samples are indicated in parentheses.

where $\text{acc}(B_m)$ is the accuracy and $\text{conf}(B_m)$ is the average confidence for a batch B_m . As the uncertainty map values are bounded between 0 and 1, we define the confidence c for each pixel as $c = 1 - u$ where u is the pixel uncertainty.

Finally, to assess if the uncertainty is predicted in the correct area, the mutual information (MI) between the uncertainty map and the pixel-wise error map computed between the mean prediction and ground truth segmentation map is computed.

2) *Clinical metrics*: For each segmentation output, we compute 4 clinical metrics: the left ventricular area (**Area**), the left-ventricular fractional area change (**FAC**), the left ventricular volume using the 2CH and 4CH views (**Volume**), and the ejection fraction (**EF**). To assess the uncertainty estimates we use the uncertainty calibration error (UCE) [37], defined by

$$\text{UCE} = \sum_{m=1}^M \frac{|B_m|}{N_{\text{test}}} |\text{err}(B_m) - \text{uncert}(B_m)|, \quad (23)$$

where $\text{err}(B_m)$ and $\text{uncert}(B_m)$ are the average error and uncertainty for a batch B_m . We define the bins to contain an equal number of samples as is used when computing adaptive calibration error [38] because the uncertainty values can have very large ranges which makes equal bin ranges likely to contain few or no samples.

In certain cases, model predictions or samples generated by various methods yield values that are clinically irrelevant. For example, due to the independent estimation of ES and ED samples, metrics such as FAC or ejection EF may result in negative values, which are not meaningful in a clinical context. Such predictions would be discarded in a clinical setting due to their irrelevance, irrespective of associated uncertainty. To ensure that these clinically irrelevant samples do not bias the uncertainty calibration error calculation, we exclude them based on the following criteria:

- 1) Reject predictions with negative values.
- 2) Discard Monte Carlo samples with negative values.
- 3) Reject a prediction if more than 50% of its Monte-Carlo samples have been discarded.

We report the percentage of rejected samples in the test set for both FAC and EF across all evaluated methods.

V. RESULTS

A. Segmentation Metrics

Segmentation results are shown in Table I. Samples showing the error and uncertainty maps used for the different metric calculations are shown in Figure 4. All methods exhibit comparable Dice scores across both datasets, with the added complexity of the private dataset leading to lower scores across methods. For uncertainty estimation, all contouring methods outperform segmentation approaches in terms of correlation between the Dice and uncertainty map mean; the highest correlation being CASUS-t.

Expected calibration error results indicate that MC Dropout and test-time augmentation have the best calibration performance. However, the pixel confidence reliability diagrams [39] in Figure 5 (col. 1) reveal that none of the segmentation methods achieve ideal calibration, as no method perfectly follows the diagonal calibration line. Most segmentation methods' lower ECE values are influenced by high-confidence bins containing the highest number of pixels, as shown in Figure 4's individual reliability diagrams. This can be explained by the behavior observed in Figure 4, showing that uncertainty is predicted just around the border of the prediction for methods like PWA and TTA. Conversely, CASUS and SSN generate more variability for all images, leading to over-estimating the uncertainty on the full dataset calibration, but resulting in better calibration for images with higher error.

Lastly, the uncertainty-error mutual information metric in Table I highlights that test-time augmentation and CASUS are the most effective in predicting uncertainty regions accurately. TTA performs better on the CAMUS dataset, where errors are smaller and predicted uncertainty aligns with errors. Conversely, on the Private dataset, where errors are more substantial, CASUS yields higher mutual information values, suggesting it captures larger errors more effectively.

Overall, adding epistemic uncertainty to aleatoric uncertainty has a minimal impact on segmentation metrics. This may be due to aleatoric uncertainty accounting for a much larger proportion of the full predictive uncertainty and that there is no specific distinction between aleatoric and epistemic uncertainty when computing the uncertainty map.

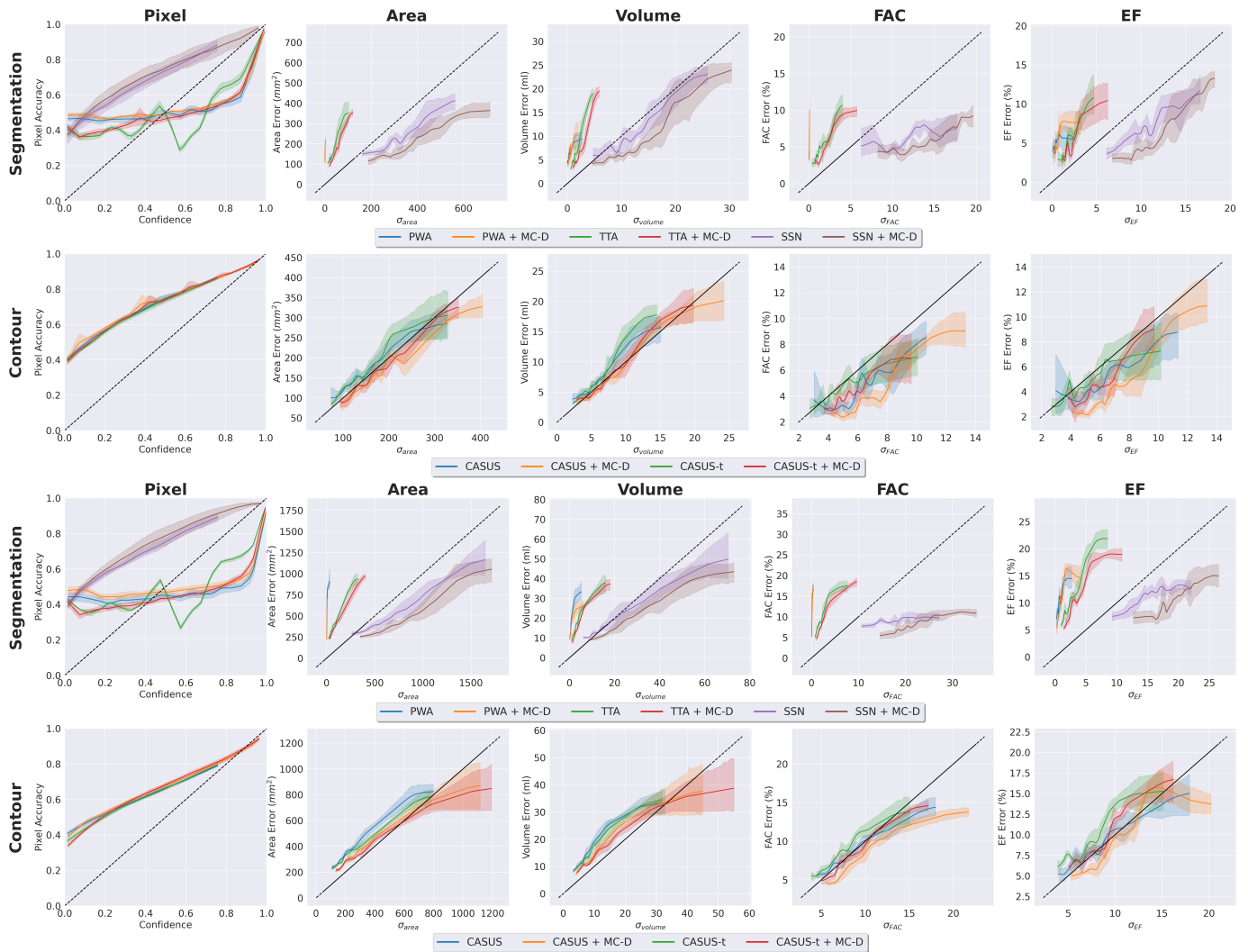


Fig. 5: Reliability diagrams for the [TOP] CAMUS and [BOTTOM] private datasets. Each row shows the calibration diagram for each aleatoric method with and without MC Dropout for each metric by column. Dashed lines indicate perfect calibration.

B. Clinical Metrics

The clinical uncertainty metric results for both the CAMUS and private datasets are summarized in Table II, with reliability diagrams displayed in Figure 5. Pixel-wise aleatoric uncertainty performs the worst, as reflected in both the metrics and reliability diagrams. This poor performance is attributed to limited variability in the generated samples, as seen in Figure 4, resulting in highly over-confident estimates. Although TTA introduces slightly more variability, it remains insufficient to achieve reliable calibration for clinical uncertainty.

Stochastic segmentation networks and CASUS variants perform similarly on area and volume metrics, with CASUS showing a slight advantage. CASUS-t, however, significantly outperforms SSN in FAC and EF metrics, as SSN lacks the ability to model temporal coherence between frames.

In contrast to segmentation metrics, modeling epistemic uncertainty substantially improves calibration for clinical metrics, especially on the private dataset where there is a larger domain shift between training and test data. When only predicting the aleatoric component of the uncertainty CASUS

shows slightly over-confident uncertainty estimates. With the addition of epistemic uncertainty, provided by MC Dropout, the predictions are almost perfectly calibrated.

CASUS+t method combined with MC-Dropout ranks as the top or second-best method across all metrics in both datasets, emphasizing the benefits of temporal consistent sampling and the inclusion of epistemic uncertainty.

VI. CONCLUSION

In this work, we presented a novel framework for uncertainty propagation in the estimation of clinical metrics from segmentations derived from echocardiographic images. This framework provides an intelligible uncertainty estimation that can combine both aleatoric and epistemic uncertainty. Although this adaptable framework accommodates any uncertainty method capable of generating samples, our findings highlight that a contour-based approach to aleatoric uncertainty, combined with shape uncertainty modeling, delivers optimal results in clinical metric calibration. This approach is further improved by integrating temporal consistency in the sampling process.

One limitation of our work is the incompatibility between the variability required to achieve clinical metric calibration and pixel-wise uncertainty calibration. The increased variability in sample generation needed for modeling clinical uncertainty leads to under-confident pixel-wise estimations. CASUS and SSN exhibit better calibration on clinical metrics but show under-confidence in pixel-wise calibration. Alternative methods for generating uncertainty maps from sample sets may further enhance calibration.

REFERENCES

- [1] A. Sánchez-Puente, P. Pérez-Sánchez, V. Vicente-Palacios, A. García-Galindo, P. P. Vara, C. Pérez del Villar, and P. L. Sánchez, "Uncertainty to improve the automatic measurement of left ventricular ejection fraction in 2d echocardiography using cnn-based segmentation," in *Functional Imaging and Modeling of the Heart*, 2023, pp. 658–667.
- [2] M. M. Kazemi Esfeh, Z. Gholami, C. Luong, T. Tsang, and P. Abolmaesumi, "Deue: Delta ensemble uncertainty estimation for a more robust estimation of ejection fraction," in *MICCAI*, 2022, pp. 525–534.
- [3] D. Behnami, Z. Liao, H. Girgis, C. Luong, R. Rohling, K. Gin, T. Tsang, and P. Abolmaesumi, "Dual-view joint estimation of left ventricular ejection fraction with uncertainty modelling in echocardiograms," in *MICCAI* 2019, 2019, pp. 696–704.
- [4] M. Ng, F. Guo, L. Biswas, S. E. Petersen, S. K. Piechnik, S. Neubauer, and G. Wright, "Estimating uncertainty in neural networks for cardiac mri segmentation: A benchmark study," *IEEE Transactions on Biomedical Engineering*, vol. 70, no. 6, pp. 1955–1966, 2023.
- [5] T. Judge, O. Bernard, M. Porumb, A. Chartsias, A. Beqiri, and P.-M. Jodoin, "Crisp - reliable uncertainty estimation for medical image segmentation," in *MICCAI*, 2022, pp. 492–502.
- [6] L. Dahal, A. Kafle, and B. Khanal, "Uncertainty estimation in deep 2d echocardiography segmentation," *CoRR*, vol. abs/2005.09349, 2020. [Online]. Available: <https://arxiv.org/abs/2005.09349>
- [7] S. Leclerc *et al.*, "Deep learning for segmentation using an open large-scale dataset in 2d echocardiography," *IEEE Transactions on Medical Imaging*, vol. 38, no. 9, pp. 2198–2210, 2019.
- [8] D. Ouyang, B. He, A. Ghorbani, N. Yuan, J. Ebinger, C. P. Langlotz, P. A. Heidenreich, R. A. Harrington, D. H. Liang, E. A. Ashley, and J. Y. Zou, "Video-based ai for beat-to-beat assessment of cardiac function," *Nature*, vol. 580, no. 7802, p. 252–256, Mar. 2020.
- [9] O. Ronneberger, P. Fischer, and T. Brox, "U-net: Convolutional networks for biomedical image segmentation," in *MICCAI*, 2015, pp. 234–241.
- [10] C. Sfakianakis, G. Simantiris, and G. Tziritas, "Gudu: Geometrically-constrained ultrasound data augmentation in u-net for echocardiography semantic segmentation," *Biomedical Signal Processing and Control*, vol. 82, p. 104557, 2023.
- [11] F. Liu, K. Wang, D. Liu, X. Yang, and J. Tian, "Deep pyramid local attention neural network for cardiac structure segmentation in two-dimensional echocardiography," *Medical Image Analysis*, vol. 67, p. 101873, 2021.
- [12] F. Isensee, P. F. Jaeger, S. A. Kohl, J. Petersen, and K. H. Maier-Hein, "nnu-net: a self-configuring method for deep learning-based biomedical image segmentation," *Nature methods*, vol. 18, no. 2, pp. 203–211, 2021.
- [13] H. J. Ling, D. Garcia, and O. Bernard, "Reaching intra-observer variability in 2-D echocardiographic image segmentation with a simple U-Net architecture," in *IEEE International Ultrasonics Symposium (IUS)*, Venice, Italy, Oct. 2022.
- [14] A. Gomez, M. Porumb, A. Mumith, T. Judge, S. Gao, W.-J. C. Kim, J. Oliveira, and A. Chartsias, "Left ventricle contouring of apical three-chamber views on 2d echocardiography," in *Simplifying Medical Ultrasound*, 2022, pp. 96–105.
- [15] N. Gaggion, L. Mansilla, C. Mosquera, D. H. Milone, and E. Ferrante, "Improving anatomical plausibility in medical image segmentation via hybrid graph neural networks: applications to chest x-ray analysis," *IEEE Transactions on Medical Imaging*, 2022.
- [16] F. Thaler, C. Payer, M. Urschler, and D. Štern, "Modeling annotation uncertainty with gaussian heatmaps in landmark localization," *Machine Learning for Biomedical Imaging*, vol. 1, pp. 1–27, 2021.
- [17] L. A. Schobs, A. J. Swift, and H. Lu, "Uncertainty estimation for heatmap-based landmark localization," *IEEE Transactions on Medical Imaging*, vol. 42, no. 4, pp. 1021–1034, 2023.
- [18] "Left ventricular ejection fraction," *Definitions*, 2020. [Online]. Available: <https://api.semanticscholar.org/CorpusID:80279998>
- [19] A. Kendall and Y. Gal, "What uncertainties do we need in bayesian deep learning for computer vision?" in *NeurIPS*, vol. 30, 2017, pp. 5574–5584.
- [20] C. Blundell, J. Cornebise, K. Kavukcuoglu, and D. Wierstra, "Weight uncertainty in neural network," in *Proceedings of the 32nd International Conference on Machine Learning*, ser. Proceedings of Machine Learning Research, vol. 37. Lille, France: PMLR, 07–09 Jul 2015, pp. 1613–1622.
- [21] "Dropout as a bayesian approximation: Representing model uncertainty in deep learning," in *Proceedings of the 33rd International Conference on International Conference on Machine Learning - Volume 48*, ser. ICML'16. JMLR.org, 2016, p. 1050–1059.
- [22] Y. Gal and Z. Ghahramani, "Bayesian convolutional neural networks with bernoulli approximate variational inference," *ArXiv*, vol. abs/1506.02158, 2015.
- [23] B. Lakshminarayanan, A. Pritzel, and C. Blundell, "Simple and scalable predictive uncertainty estimation using deep ensembles," in *NeurIPS*, vol. 30, 2017.
- [24] R. L. Russell and C. Reale, "Multivariate uncertainty in deep learning," *IEEE Transactions on Neural Networks and Learning Systems*, vol. 33, no. 12, pp. 7937–7943, 2022.
- [25] T. Judge, O. Bernard, W.-J. Cho Kim, A. Gomez, A. Chartsias, and P.-M. Jodoin, "Asymmetric contour uncertainty estimation for medical image segmentation," in *MICCAI*, 2023, pp. 210–220.
- [26] M. S. Ayhan and P. Berens, "Test-time data augmentation for estimation of heteroscedastic aleatoric uncertainty in deep neural networks," in *International conference on Medical Imaging with Deep Learning*, 2018.
- [27] S. Kohl, B. Romera-Paredes, C. Meyer, J. De Fauw, J. R. Ledsam, K. Maier-Hein, S. M. A. Eslami, D. Jimenez Rezende, and O. Ronneberger, "A probabilistic u-net for segmentation of ambiguous images," in *NeurIPS*, vol. 31, 2018.
- [28] C. F. Baumgartner, K. C. Tezcan, K. Chaitanya, A. M. Hötter, U. J. Muehlematter, K. Schawkat, A. S. Becker, O. Donati, and E. Konukoglu, "Phiseg: Capturing uncertainty in medical image segmentation," in *MICCAI*, 2019, pp. 119–127.
- [29] M. Monteiro, L. Le Folgoc, D. Coelho de Castro, N. Pawlowski, B. Marques, K. Kamnitsas, M. van der Wilk, and B. Glocker, "Stochastic segmentation networks: Modelling spatially correlated aleatoric uncertainty," in *NeurIPS*, vol. 33, 2020, pp. 12756–12767.
- [30] G. Wang, W. Li, M. Aertsen, J. Deprest, S. Ourselin, and T. Vercauteren, "Aleatoric uncertainty estimation with test-time augmentation for medical image segmentation with convolutional neural networks," *Neurocomputing*, vol. 338, pp. 34–45, 2019.
- [31] M. H. Jafari, N. V. Woudenberg, C. Luong, P. Abolmaesumi, and T. Tsang, "Deep bayesian image segmentation for a more robust ejection fraction estimation," in *2021 IEEE 18th International Symposium on Biomedical Imaging (ISBI)*, 2021, pp. 1264–1268.
- [32] A. Nibali, Z. He, S. Morgan, and L. Prendergast, "Numerical coordinate regression with convolutional neural networks," *arXiv preprint arXiv:1801.07372*, 2018.
- [33] T. Albrecht, M. Lüthi, T. Gerig, and T. Vetter, "Posterior shape models," *Medical Image Analysis*, vol. 17, no. 8, pp. 959–973, 2013.
- [34] W. Woodward, C. Dockerill, A. McCourt, R. Upton, J. O'Driscoll, K. Balkhausen, B. Chandrasekaran, S. Firoozan, A. Kardos, K. Wong *et al.*, "Real-world performance and accuracy of stress echocardiography: the evarest observational multi-centre study," *European Heart Journal-Cardiovascular Imaging*, vol. 23, no. 5, pp. 689–698, 2022.
- [35] D. P. Kingma and J. Ba, "Adam: A method for stochastic optimization," in *3rd International Conference on Learning Representations, ICLR 2015, San Diego, CA, USA, May 7-9, 2015, Conference Track Proceedings*, 2015.
- [36] M. Pakdaman Naeini, G. Cooper, and M. Hauskrecht, "Obtaining well calibrated probabilities using bayesian binning," *Proceedings of the AAAI Conference on Artificial Intelligence*, vol. 29, no. 1, Feb. 2015.
- [37] M.-H. Laves, S. Ihler, J. F. Fast, L. A. Kahrs, and T. Ortmaier, "Well-calibrated regression uncertainty in medical imaging with deep learning," in *Proceedings of the Third Conference on Medical Imaging with Deep Learning*, ser. Proceedings of Machine Learning Research, vol. 121. PMLR, 06–08 Jul 2020, pp. 393–412.
- [38] J. Nixon, M. W. Dusenberry, L. Zhang, G. Jerfel, and D. Tran, "Measuring calibration in deep learning," in *Proceedings of the IEEE/CVF Conference on Computer Vision and Pattern Recognition (CVPR) Workshops*, June 2019.
- [39] A. Niculescu-Mizil and R. Caruana, "Predicting good probabilities with supervised learning," in *Proceedings of the 22nd International Conference on Machine Learning*, ser. ICML '05. New York, NY, USA: Association for Computing Machinery, 2005, p. 625–632.